

A Semi-Implicit Meshless Method for Incompressible Flows in Complex Geometries

Shantanu Shahane¹, Surya Pratap Vanka

*Department of Mechanical Science and Engineering,
University of Illinois at Urbana-Champaign, Urbana, Illinois 61801*

Abstract

We present an exponentially convergent semi-implicit meshless algorithm for the solution of Navier-Stokes equations in complex domains. The algorithm discretizes partial derivatives at scattered points using radial basis functions as interpolants. Higher-order polynomials are appended to polyharmonic splines (PHS-RBF) and a collocation method is used to derive the interpolation coefficients. The interpolating kernels are then differentiated and the partial-differential equations are satisfied by collocation at the scattered points. The PHS-RBF interpolation is shown to be exponentially convergent with discretization errors decreasing as a high power of a representative distance between points. We present here a semi-implicit algorithm for time-dependent and steady state fluid flows in complex domains. At each time step, several iterations are performed to converge the momentum and continuity equations. A Poisson equation for pressure corrections is formulated by imposing divergence free condition on the iterated velocity field. At each time step, the momentum and pressure correction equations are repeatedly

¹Corresponding Author Email Address: shahaneshantanu@gmail.com

solved until the velocities and pressure converge to a pre-specified tolerance. We have demonstrated the convergence and discretization accuracy of the algorithm for two model problems and simulated three other complex problems. In all cases, the algorithm is stable for Courant numbers in excess of ten. The algorithm has the potential to accurately and efficiently solve many fluid flow and heat transfer problems in complex domains. An open source code Meshless Multi-Physics Software (MeMPhyS) [1] is available for interested users of the algorithm.

Keywords: Meshless method, Radial Basis Function based Finite Difference, Polyharmonic Spline, Semi-Implicit Method, Incompressible Navier-Stokes Equation

1. Introduction

Numerical algorithms to solve the coupled Navier-Stokes equations for incompressible flows can be categorized as: i) time marching pressure-projection methods [2–7], ii) semi-implicit equation-by-equation decoupled iterative schemes [8–12], or fully-coupled block-implicit methods using Newton methods for the coupled nonlinear discrete equations [13–17]. The appropriate technique for a given flow depends on the flow characteristics and the desired temporal information from the numerical solution. The explicit fractional step (pressure-projection) methods are ideal for problems with needs to accurately calculate the flow instabilities and turbulent fluctuations, such as in Direct and Large-eddy Simulations (DNS and LES) of turbulence [18–22]. In such explicit methods for incompressible Navier-Stokes equations, the time step is based on a combination of velocity and diffusion Courant numbers or only

on the velocity Courant number, if the diffusion terms are treated implicitly. A number of variants of pressure-projection methods with second-order temporal accuracy have been developed in combination with finite-difference, finite-volume, spectral and spectral-element methods [23–27].

If the temporal variations are not fast (slow transients), or only the steady state flow fields are desired, one can use a semi-implicit method in which the time-dependent equations are solved with larger time steps (several times the velocity Courant number) with iterations over the coupled equations at each time step. For steady state problems, the temporally evolving solution is of interest only in passing, and therefore, moderate temporal errors can be accepted. An alternative to time marching is a direct relaxation method of the coupled equations using an iterative correction strategy. Such a strategy is followed in the well-known SIMPLE series [10, 11] of algorithms where, a pressure-correction equation is derived from truncated discrete momentum equations to satisfy the divergence-free condition on the velocities. A number of different pressure-correction strategies [8, 9, 12] have been proposed as an improvement to the original SIMPLE algorithm. Since the momentum equations are nonlinear, an iterative method is always needed. Several works [13–17] have combined Newton type methods with coupled direct or iterative solvers to efficiently solve the discrete equations. If the initial guess is reasonably good, the coupled solvers converge rapidly in a small number of iterations. However, coupled direct solvers are not attractive for large numbers of nonlinear equations usually required for industrial flow simulations. Iterative methods for such coupled equations combining Krylov subspace methods [28, 29] and multigrid techniques [30–32] have also been pursued.

Recently, there has been growing interest in solving the Navier-Stokes equations in complex domains using meshless methods that discretize the governing partial differential equations using only scattered points. Among the several types of meshless methods [33–39], interpolation with radial basis functions provides a novel way to construct discrete forms of the Navier Stokes equations [40–48]. Several RBFs have been previously used for such interpolation of values at scattered locations [49]. These include:

$$\begin{aligned}
&\text{Multiquadrics (MQ): } \phi(r) = (r^2 + \epsilon^2)^{1/2} \\
&\text{Inverse Multiquadrics (IMQ): } \phi(r) = (r^2 + \epsilon^2)^{-1/2} \\
&\text{Gaussian: } \phi(r) = \exp\left(\frac{-r^2}{\epsilon^2}\right) \tag{1} \\
&\text{Polyharmonic Splines (PHS): } \phi(r) = r^{2a+1}, \quad a \in \mathbb{N} \\
&\text{Thin Plate Splines (TPS): } \phi(r) = r^{2a} \log(r), \quad a \in \mathbb{N}
\end{aligned}$$

The PHS-RBF interpolation has the advantage over MQ, IMQ and Gaussians of not requiring a shape factor. The value of this shape factor is not known precisely, but the accuracy of interpolation as well as the condition number of the matrix required to determine the interpolation coefficients strongly depend on the shape factor. The RBF interpolations can also be appended with polynomials to get high accuracy. It has been demonstrated earlier [45, 49, 50] that when the RBFs are appended with polynomials and the derivatives of a smooth function are evaluated, the discretization errors converge exponentially per the degree of the appended polynomial. RBFs have been originally used as global interpolants of scattered data [51] and to solve partial differential equations [52–54], but the size of the problem has

been limited because of the condition number of the solution matrix. Cloud based methods [40, 41], on the other hand, are attractive because of the lower condition number and sparsity of the coefficient matrix. PHS-RBF methods with appended polynomials have been used in the past to solve several partial differential equations, including the Navier Stokes equations. Recently, we presented [45] a pressure-projection based algorithm using PHS-RBF to solve the time-dependent Navier Stokes equations of an incompressible flow. We presented the spatial discretization accuracy of the method in several problems by systematically varying the appended polynomial and the numbers of scattered points. That algorithm used an explicit formulation of the advection and diffusion terms using an Adams-Bashforth discretization in time. The divergence-free condition on the velocities was imposed by solving a pressure Poisson equation. Such explicit methods are well-suited for problems in which rapid transients are to be resolved, such as in simulations of turbulence. However, they are not optimal to compute steady state flows, and time-varying flows which permit large timesteps from accuracy viewpoint. For such needs, semi-implicit methods that permit several multiples of the velocity Courant number can be faster in solution time. Semi-implicit methods iterate between the momentum and continuity equations until desired convergence is obtained at each time step. Although the computational cost per timestep increases due to the iterations, overall this approach is efficient because the number of timesteps to reach a stationary solution is reduced significantly.

In this paper, we describe a semi-implicit PHS-RBF meshless method which is attractive to compute steady as well as temporally evolving flows.

The method can use time steps significantly larger than the time step restricted by an explicit algorithm. We first present the convergence characteristics of the method in several model flows. Subsequently, the algorithm is applied to compute three complex steady and unsteady recirculating flows.

2. The PHS-RBF Discretization

The Navier-Stokes equations consist of differential operators of first and second order. In this work, PHS-RBF expansions collocated over a cloud of neighboring points are used to numerically estimate these differential operators. Monomials upto a maximum degree k are appended for stabilization and accuracy of the PHS functions. A continuous scalar variable s can be interpolated over q cloud points as follows:

$$s(\mathbf{x}) = \sum_{i=1}^q \lambda_i \phi_i(\|\mathbf{x} - \mathbf{x}_i\|_2) + \sum_{i=1}^m \gamma_i P_i(\mathbf{x}) \quad (2)$$

where, $\phi(r) = r^{2a+1}$, $a \in \mathbb{N}$. In this work, we use the PHS-RBF $\phi(r) = r^3$. There are total $q + m$ unknowns (λ_i and γ_i) to be estimated. Collocating eq. (2) at the q cloud points gives q conditions. Additional m equations are obtained by imposing the following constraints on the polynomials [49]:

$$\sum_{i=1}^q \lambda_i P_j(\mathbf{x}_i) = 0 \quad \text{for } 1 \leq j \leq m \quad (3)$$

The collocation conditions together with eq. (3) can be written in a matrix vector form,

$$\begin{bmatrix} \mathbf{\Phi} & \mathbf{P} \\ \mathbf{P}^T & \mathbf{0} \end{bmatrix} \begin{bmatrix} \boldsymbol{\lambda} \\ \boldsymbol{\gamma} \end{bmatrix} = \begin{bmatrix} \mathbf{A} \end{bmatrix} \begin{bmatrix} \boldsymbol{\lambda} \\ \boldsymbol{\gamma} \end{bmatrix} = \begin{bmatrix} \mathbf{s} \\ \mathbf{0} \end{bmatrix} \quad (4)$$

where, the superscript T denotes the transpose, $\boldsymbol{\lambda} = [\lambda_1, \dots, \lambda_q]^T$, $\boldsymbol{\gamma} = [\gamma_1, \dots, \gamma_m]^T$, $\mathbf{s} = [s(\mathbf{x}_1), \dots, s(\mathbf{x}_q)]^T$ and $\mathbf{0}$ is the matrix of zeros. Sizes of the submatrices \mathbf{P} and $\mathbf{\Phi}$ are $q \times m$ and $q \times q$ respectively. The submatrix $\mathbf{\Phi}$ is given by:

$$\mathbf{\Phi} = \begin{bmatrix} \phi(\|\mathbf{x}_1 - \mathbf{x}_1\|_2) & \dots & \phi(\|\mathbf{x}_1 - \mathbf{x}_q\|_2) \\ \vdots & \ddots & \vdots \\ \phi(\|\mathbf{x}_q - \mathbf{x}_1\|_2) & \dots & \phi(\|\mathbf{x}_q - \mathbf{x}_q\|_2) \end{bmatrix} \quad (5)$$

For two dimensional problem ($d = 2$) with maximum degree of appended polynomial set to 2 ($k = 2$), there are $m = \binom{k+d}{k} = \binom{2+2}{2} = 6$ polynomial terms: $[1, x, y, x^2, xy, y^2]$. Thus, the submatrix \mathbf{P} is obtained by evaluating the polynomial terms at the q cloud points.

$$\mathbf{P} = \begin{bmatrix} 1 & x_1 & y_1 & x_1^2 & x_1 y_1 & y_1^2 \\ \vdots & \vdots & \vdots & \vdots & \vdots & \vdots \\ 1 & x_q & y_q & x_q^2 & x_q y_q & y_q^2 \end{bmatrix} \quad (6)$$

Unknown interpolation coefficients λ_i and γ_i are obtained by solving the eq. (4):

$$\begin{bmatrix} \boldsymbol{\lambda} \\ \boldsymbol{\gamma} \end{bmatrix} = \begin{bmatrix} \mathbf{A} \end{bmatrix}^{-1} \begin{bmatrix} \mathbf{s} \\ \mathbf{0} \end{bmatrix} \quad (7)$$

In eq. (7), the inverse of matrix \mathbf{A} is used as a notation. Practically, the equation is solved by a direct linear solver.

The differential operators in the Navier-Stokes equation are estimated as a weighted linear summation of the function values at the neighboring cloud points. Applying any scalar linear operator \mathcal{L} such as $\frac{\partial}{\partial x}$ or the Laplacian ∇^2 on eq. (2) gives:

$$\mathcal{L}[s(\mathbf{x})] = \sum_{i=1}^q \lambda_i \mathcal{L}[\phi_i(\|\mathbf{x} - \mathbf{x}_i\|_2)] + \sum_{i=1}^m \gamma_i \mathcal{L}[P_i(\mathbf{x})] \quad (8)$$

Equation (8) is collocated by evaluating $\mathcal{L}[s]$ at the q cloud points. This gives a rectangular matrix vector system:

$$\mathcal{L}[s] = \begin{bmatrix} \mathcal{L}[\Phi] & \mathcal{L}[P] \end{bmatrix} \begin{bmatrix} \lambda \\ \gamma \end{bmatrix} \quad (9)$$

where, $\mathcal{L}[P]$ and $\mathcal{L}[\Phi]$ are matrices of sizes $q \times m$ and $q \times q$ respectively. Substituting eq. (7) in eq. (9) and simplifying, we get:

$$\begin{aligned} \mathcal{L}[s] &= \left(\begin{bmatrix} \mathcal{L}[\Phi] & \mathcal{L}[P] \end{bmatrix} [\mathbf{A}]^{-1} \right) \begin{bmatrix} s \\ \mathbf{0} \end{bmatrix} = [\mathbf{B}] \begin{bmatrix} s \\ \mathbf{0} \end{bmatrix} \\ &= \begin{bmatrix} \mathbf{B}_1 & \mathbf{B}_2 \end{bmatrix} \begin{bmatrix} s \\ \mathbf{0} \end{bmatrix} = [\mathbf{B}_1][s] + [\mathbf{B}_2][\mathbf{0}] = [\mathbf{B}_1][s] \end{aligned} \quad (10)$$

Thus, $\mathcal{L}[s]$ at any point is estimated using the weighted summation of the values of s at its neighboring cloud points. The matrix $[\mathbf{B}_1]$ in eq. (10) is precomputed using the coordinates of the cloud points and stored for use

throughout the solution steps. Properties of the PHS-RBF expansion are reported in our previous publication [45].

3. Semi-Implicit Solution Algorithm

We have previously reported a fully explicit fractional step algorithm with the PHS-RBF method to solve the incompressible Navier-Stokes equations [45]. This explicit method is computationally expensive since the time step is limited by the condition that the convection and diffusion Courant number be less than unity. In this work, we describe a semi-implicit iterative algorithm which is shown to be stable for Courant numbers much higher than unity. For temporal discretization, we use a second-order accurate backward differentiation formula (BDF2) [55] which expresses the momentum equations as

$$\frac{\rho(\alpha_1 u^{n+1} + \alpha_2 u^n + \alpha_3 u^{n-1})}{\Delta t} = -\rho \mathbf{u}^{n+1} \bullet (\nabla u^{n+1}) + \mu \nabla^2 u^{n+1} - \left(\frac{\partial p}{\partial x} \right)^{n+1} \quad (11)$$

$$\frac{\rho(\alpha_1 v^{n+1} + \alpha_2 v^n + \alpha_3 v^{n-1})}{\Delta t} = -\rho \mathbf{u}^{n+1} \bullet (\nabla v^{n+1}) + \mu \nabla^2 v^{n+1} - \left(\frac{\partial p}{\partial y} \right)^{n+1} \quad (12)$$

where, n is timestep number, ρ is density, μ is dynamic viscosity, $\mathbf{u} = [u, v]$ is velocity vector, p is pressure and $\alpha_1 = 1.5$, $\alpha_2 = -2$ and $\alpha_3 = 0.5$ are the BDF2 coefficients [55]. The incompressible continuity equation is evaluated

at the new timestep $n + 1$ as

$$\left(\frac{\partial u}{\partial x}\right)^{n+1} + \left(\frac{\partial v}{\partial y}\right)^{n+1} = 0 \quad (13)$$

Equations (11) and (12) have to be solved iteratively since the convection terms are nonlinear and p^{n+1} is unknown. Given the $[u^n, v^n, p^n]$ and $[u^{n-1}, v^{n-1}, p^{n-1}]$ values at the previous two timesteps, the algorithm iterates to solve for $[u^{n+1}, v^{n+1}, p^{n+1}]$ as follows. First, the advection terms are linearized with previous iterate values and the diffusion terms are expressed implicitly at the current iteration. Together with the old iterate pressure gradients, we solve:

$$\frac{\rho(\alpha_1 \tilde{u} + \alpha_2 u^n + \alpha_3 u^{n-1})}{\Delta t} = -\rho \mathbf{u}^r \bullet (\nabla \tilde{u}) + \mu \nabla^2 \tilde{u} - \left(\frac{\partial p}{\partial x}\right)^r \quad (14)$$

$$\frac{\rho(\alpha_1 \tilde{v} + \alpha_2 v^n + \alpha_3 v^{n-1})}{\Delta t} = -\rho \mathbf{u}^r \bullet (\nabla \tilde{v}) + \mu \nabla^2 \tilde{v} - \left(\frac{\partial p}{\partial y}\right)^r \quad (15)$$

where, \tilde{u} and \tilde{v} denote intermediate velocity fields. The spatial derivatives are expressed as a weighted linear combination of the velocities and pressure at the cloud points as discussed in section 2. Equations (14) and (15) are solved for \tilde{u} and \tilde{v} using a preconditioned BiCGSTAB algorithm. We then correct the pressure field by approximately relating the velocity corrections to the corrections of pressure gradients.

$$\frac{\rho \alpha_1 (u^{r+1} - \tilde{u})}{\Delta t} \approx -\frac{\partial (p^{r+1} - p^r)}{\partial x} = -\frac{\partial p'}{\partial x} \quad (16)$$

$$\frac{\rho\alpha_1(v^{r+1} - \tilde{v})}{\Delta t} \approx -\frac{\partial(p^{r+1} - p^r)}{\partial y} = -\frac{\partial p'}{\partial y} \quad (17)$$

where, p' denotes pressure corrections. Note that in the above approximation, we have neglected the changes in the advection and diffusion terms. Imposing the divergence-free condition on the velocity field at the new iteration ($r + 1$) gives the Poisson equation for pressure corrections:

$$\nabla^2 p' = \frac{\rho\alpha_1}{\Delta t} \left(\frac{\partial \tilde{u}}{\partial x} + \frac{\partial \tilde{v}}{\partial y} \right) \quad (18)$$

The pressure-correction equation is also discretized with high accuracy using the PHS-RBF discretization scheme and solved with a preconditioned BiCGSTAB algorithm to a pre-specified tolerance. After the pressure-corrections are determined, the velocities and pressures are corrected as

$$u^{r+1} = \tilde{u} - \frac{\Delta t}{\rho\alpha_1} \left(\frac{\partial p'}{\partial x} \right) \quad (19)$$

$$v^{r+1} = \tilde{v} - \frac{\Delta t}{\rho\alpha_1} \left(\frac{\partial p'}{\partial y} \right) \quad (20)$$

Similarly, the pressure is corrected as:

$$p^{r+1} = p^r + p' \quad (21)$$

Note that the above algorithm has similarities to the SIMPLE series of algorithms [12], but here the pressure correction equation is formulated only through the time-dependent term in the momentum equations whereas, SIM-

PLE formulates the p' equation from truncated discretized momentum equations with only the diagonal terms. In situations where time-dependent problems are solved with SIMPLE, the contributions of the time-dependent terms are added to the diagonal coefficients. The present algorithm is more straightforward in deriving the pressure-correction equation. Also, we do not use any under-relaxation factors in any of the equations. The time-dependent term provides the needed damping to the nonlinearities and the coupling terms.

3.1. Boundary Conditions

The present algorithm is compatible with most of the boundary conditions used in practical flow conditions. These include Dirichlet, Neumann and periodic boundary conditions. At inlet and wall boundaries, the velocities are specified to be the known values. These velocities are either fixed in time or can be varied depending on the problem. The values of these velocities are also imposed on the \tilde{u} and \tilde{v} velocities of eqs. (14) and (15). At symmetry boundaries, the normal velocities are prescribed to be zero and the tangential velocities at the boundaries are determined by implicitly imposing zero normal derivatives. Derivatives at the boundary points are discretized over a local cloud surrounding the boundary points. The pressures at the boundary points are determined by imposing the normal momentum equation given by

$$\nabla p \bullet \widehat{\mathbf{N}} = \left[-\rho \left(\frac{\partial \mathbf{u}}{\partial t} \right) - \rho (\mathbf{u} \bullet \nabla) \mathbf{u} + \mu \nabla^2 \mathbf{u} \right] \bullet \widehat{\mathbf{N}} \quad (22)$$

These boundary pressures are required for evaluating the pressure-gradients appearing in the momentum equations. In the solution of the pressure correction equation however, homogeneous Neumann conditions ($\partial p' / \partial \widehat{\mathbf{N}} = 0$)

are imposed at the walls, inlet, and symmetry boundaries. For boundaries with prescribed pressure, the pressure corrections are specified to be zero. The outlet boundary can be prescribed to be either fixed pressure or have zero normal derivatives on the velocities. The relevant derivatives are computed in Cartesian coordinates and resolved appropriately in the direction normal to the boundary. Note that only one-sided cloud points are used at all boundaries.

Lastly, we have also implemented periodicity boundary conditions in any one or both the spatial directions. Periodicity implies repeated domain with same velocities and pressures. Thus, the variables are wrapped around in the periodic direction. Figure 1 shows a schematic of the cloud definitions at the periodic and non-periodic boundaries. The periodic boundary is imposed implicitly by defining clouds for near boundary points that include some points adjacent to the boundary from the other end of the domain. Thus, for periodic boundary conditions, the clouds are much like any interior point shown in the center of fig. 1. This contrasts with the asymmetric cloud of points at a non-periodic boundary point. For periodic flows, such as a fully-developed flow in a channel, a mean pressure gradient is provided as an additional forcing term in the direction of periodicity. The governing equations are solved on the points near a periodic boundary and thus, no boundary condition is required. For this case, the two sides of the domain are coupled with each other.

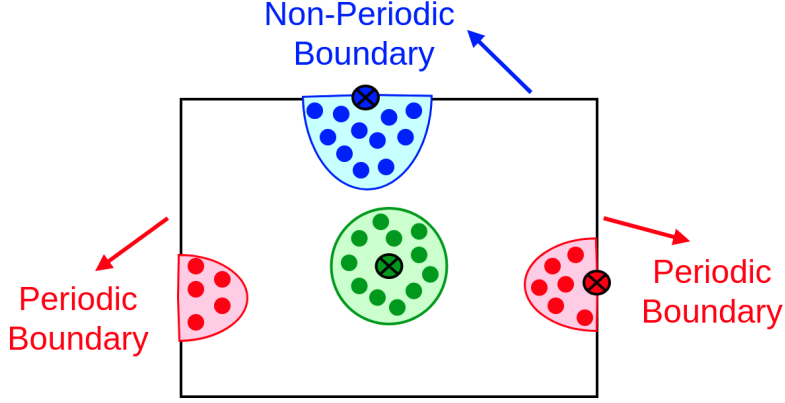


Figure 1: Clouds for Interior (Green), Periodic (Red) and Non-Periodic (Blue) Boundaries

3.2. Summary of Solution Steps

The steps in the present solution algorithm for time marching from timesteps $n - 1$ and n to $n + 1$ can be summarized as follows:

1. Initialize the values at the iteration number $r = 0$ as $[u^r, v^r, p^r] = [u^n, v^n, p^n]$
2. Solve eqs. (14) and (15) for intermediate velocities (\tilde{u} and \tilde{v}) with the appropriate boundary condition (section 3.1) using any linear solver such as a preconditioned BiCGSTAB solver
3. Solve the Poisson eq. (18) for pressure correction (p')
4. Correct the pressure to estimate p^{r+1} at the interior points (eq. (21))
5. Set the pressure at the boundary points using the normal momentum eq. (22)
6. Update the velocities at the new iteration (u^{r+1} and v^{r+1}) using the velocity correction eqs. (19) and (20)
7. Compute the change during the current iteration: $\Delta = \|u^{r+1} - u^r\| + \|v^{r+1} - v^r\|$

8. If Δ is less than the prescribed iterative tolerance, set $[u^{n+1}, v^{n+1}, p^{n+1}] = [u^{r+1}, v^{r+1}, p^{r+1}]$ and proceed to a new timestep. Otherwise, go back to step 2

We calculate the Courant number from the eigenvalues of the matrix corresponding to the discrete convection and diffusion operators. The Courant number given by $\lambda_{rmax}\Delta t/2$ is kept to be less than unity for first order explicit Euler method where, λ_{rmax} denotes the eigenvalue with the maximum real component [56]. In the semi-implicit method with BDF2, we can have Courant numbers much greater than unity. We have successfully tested the semi-implicit algorithm with BDF2 for time integration upto a Courant number of 12. For the problems studied in this paper, we observed that at each time step typically 2-3 iterations have been necessary to obtain a good convergent solution. However, the first few timesteps (around 20) may require 5 or 10 outer iterations. We initially set an iterative tolerance of $1E-4$. For subsequent timesteps, the tolerance is updated as: $\min[1E-4, \Delta t\epsilon_s]$ where, $\epsilon_s = \frac{\phi^{n+1}-\phi^n}{\Delta t}$ is the rate of change in the velocity fields at consecutive timesteps denoted by ϕ^{n+1} and ϕ^n . As steady state is approached ϵ_s reduces and thus, the term $\Delta t\epsilon_s$ tightens the iterative tolerance.

4. Convergence Characteristics in Model Problems

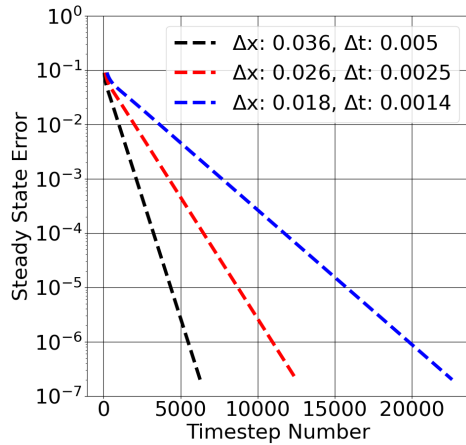
4.1. Steady Cylindrical Couette Flow

We have first studied the convergence characteristics in cylindrical Couette flow to test the convergence of the algorithm as well as the discretization errors at steady state. Cylindrical Couette flow is a one dimensional

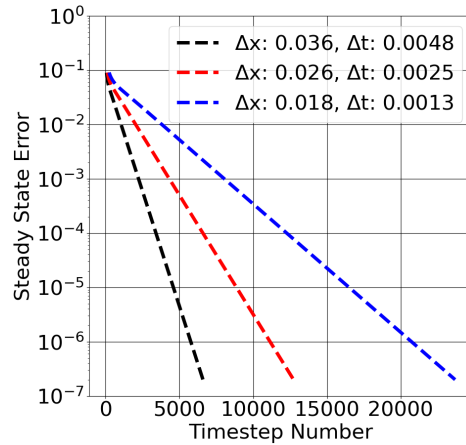
problem in cylindrical polar coordinates but here, it is solved as a two dimensional problem in Cartesian coordinates. The annular region between the two cylinders is filled with fluid with inner cylinder rotating and outer cylinder stationary. The tangential velocity as a function of radial coordinate (r) is analytically given by:

$$v_{\theta}(r) = r_1\omega \frac{r_1r_2}{r_2^2 - r_1^2} \left(\frac{r_2}{r} - \frac{r}{r_2} \right) \quad (23)$$

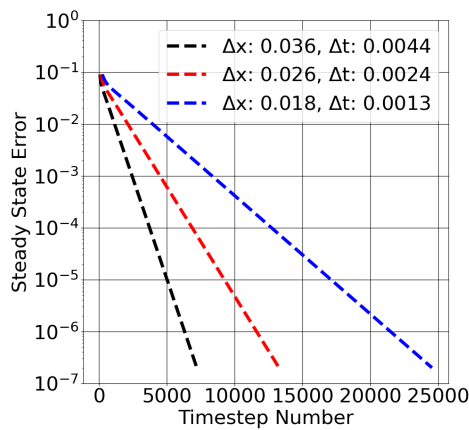
where, ω , r_1 and r_2 are rotational velocity of the inner cylinder, inner and outer radii respectively. This tangential velocity is decomposed into velocity fields in the Cartesian X and Y directions. At low rotational Reynolds number, the flow does not develop into longitudinal Taylor vortices and it remains steady and laminar. The flow Reynolds number defined with respect to inner cylinder's diameter and its tangential velocity is set to 100 although, the velocity field is independent of the Reynolds number. We have prescribed a rotational velocity of $\omega = 2$, $r_1 = 0.5$ and $r_2 = 1$. Three different points distributions having 2080, 4033 and 8078 points are used with four increasing degrees of appended polynomials 3, 4, 5 and 6. These point distributions correspond to Δx of 0.036, 0.026 and 0.018 respectively. Δx is defined as the average value of the distance between each point and its nearest neighbor. Steady state solution is obtained by integrating in time from null velocity and pressure fields. Steady state error is defined as $\frac{\phi^{n+1} - \phi^n}{\Delta t}$ where, ϕ denotes X and Y components of velocity evaluated at consecutive timesteps n and $n + 1$. When the spatial average of the above error reaches a tolerance of 2E-7 for X and Y velocity components, the time integration is stopped.



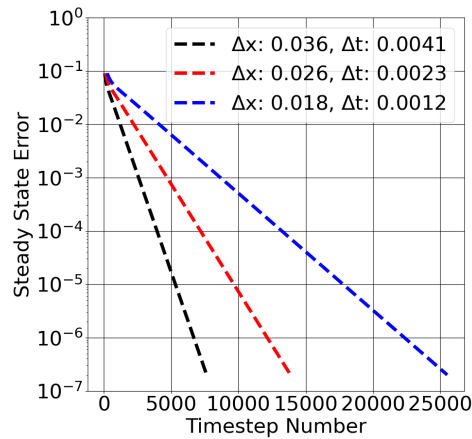
(a) Polynomial Degree 3



(b) Polynomial Degree 4



(c) Polynomial Degree 5

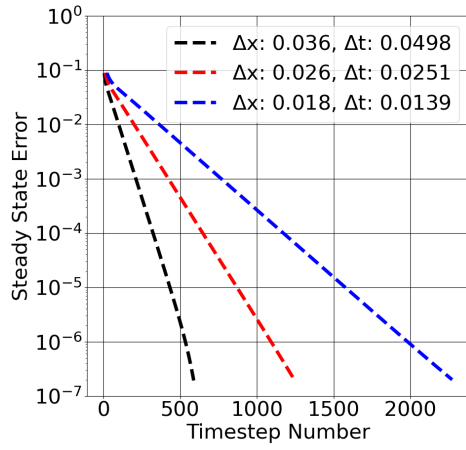


(d) Polynomial Degree 6

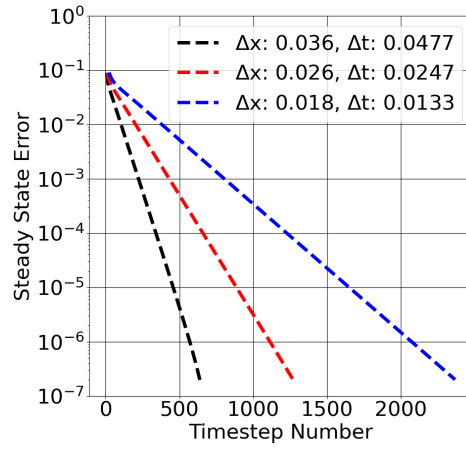
Figure 2: Convergence of the Fractional Step Algorithm [45]: Courant No.: 0.8

For comparison, first we simulate using the fractional step method at a Courant number of 0.8 [45]. Since the stability is a function of the weighted sum of the eigenvalues of the discrete convection and diffusion operators, we see that when Δx reduces by a factor of 2 from 0.036 to 0.018, the timestep Δt reduces approximately by a factor of 3.5. The timestep only marginally reduces when the polynomial degree is increased for the same

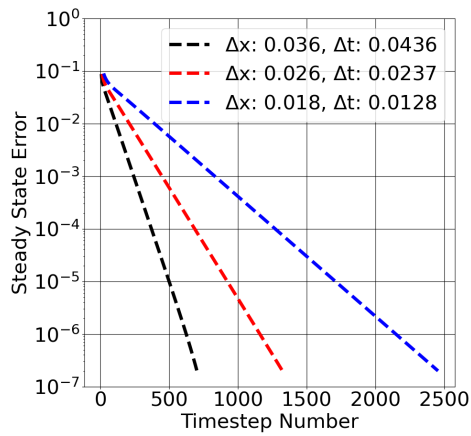
Δx . For problems having steady state, we have used first order explicit Euler method for time integration in the fractional step algorithm [45]. Figure 2 plots the temporal evolution of the steady state error using the fractional step method. The steady state error drops at a constant rate on a logarithmic scale with timestep. The number of timesteps needed to reach steady state are inversely proportional to Δt thus, coarser point distributions converge faster. Figures 3 and 4 plot errors for the current semi-implicit algorithm with Courant numbers of 8 and 12 respectively. This case shows a steeper drop in the steady state errors compared to fig. 2. Thus, the steady state is reached in less number of timesteps as expected. These plots show the computational advantage of the semi-implicit algorithm over the previous explicit fractional step method.



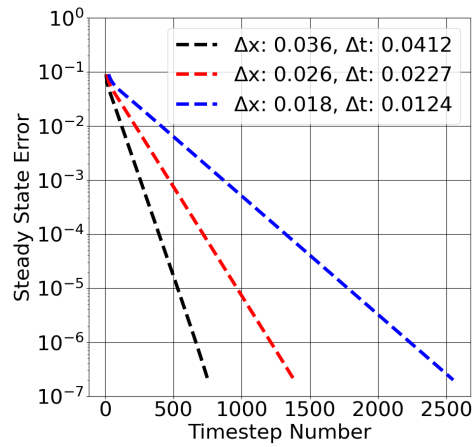
(a) Polynomial Degree 3



(b) Polynomial Degree 4



(c) Polynomial Degree 5



(d) Polynomial Degree 6

Figure 3: Convergence of the Semi-Implicit Algorithm: Courant No.: 8

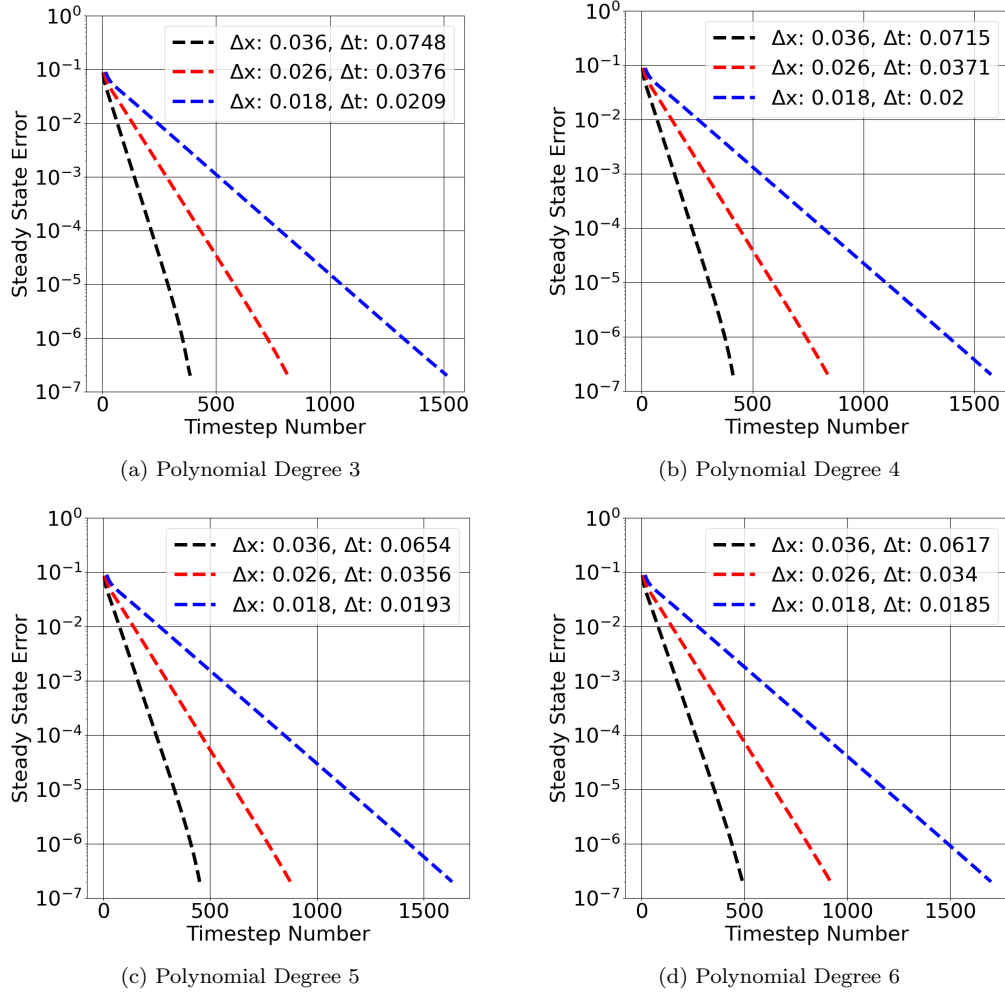


Figure 4: Convergence of the Semi-Implicit Algorithm: Courant No.: 12

Figure 5 compares CPU runtimes for the finest point distribution. The red colored bar plots runtime for the fractional step algorithm. The green and blue bars are for the semi-implicit algorithm with Courant numbers of 8 and 12 respectively. All calculations used the same compilers and computer hardware. For each polynomial degree, the speedup is defined as the ratio of runtime of the fractional step to the semi-implicit algorithm. Thus, the

speedup for the fractional step is unity whereas, for the semi-implicit method, it is in the range [3.6, 4.5] and [5.0, 6.0] for the Courant numbers of 8 and 12 respectively.

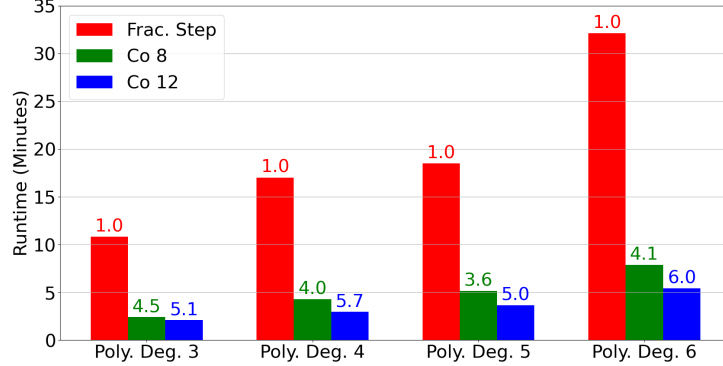
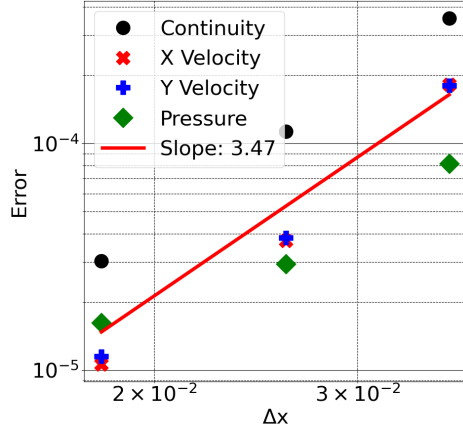


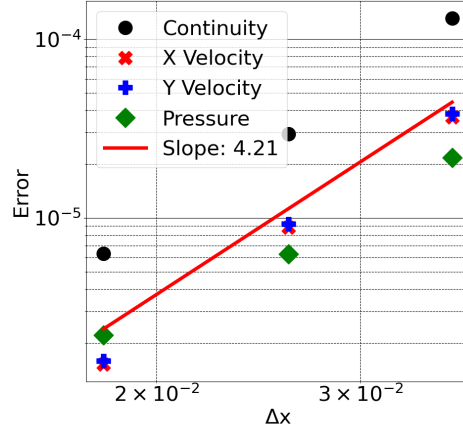
Figure 5: CPU Runtime with Speedup Factors for 8078 points with $\Delta x = 0.018$

For transient cases, we find that each timestep of the semi-implicit algorithm converges in 3 to 4 outer iterations for a tolerance of $1E-4$. The fractional step algorithm with second-order accurate Adams Bashforth differencing requires a Courant number of 0.5 or less. Hence with a Courant number of 12, the semi-implicit algorithm is 6 to 8 times faster over the fractional step algorithm when transient problems are of interest. However, because of the larger time step in the semi-implicit algorithm the temporal errors can be larger than those in the fractional step algorithm, depending on the transient. Note that although we have used a maximum Courant number of 12 in this paper, it is not a hard limit. We have observed the algorithm to be stable up to Courant numbers of 50 in some problems. However, at large Courant numbers there may be some minor oscillations in convergence. Hence, a value of Courant number around 12 is used for both steady and transient problems considered in this paper.

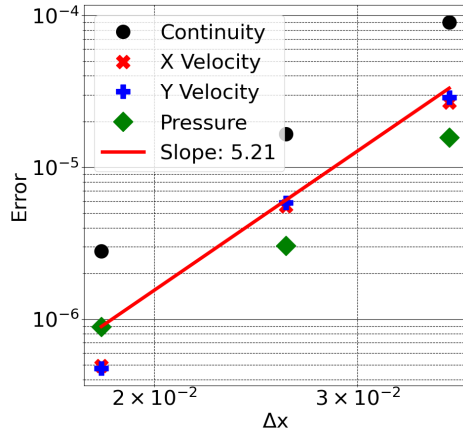
As shown previously by Shahane et al. [45] for the fractional step algorithm, the PHS basis functions and appended polynomials give high order convergence of the discretization errors. We expect the same behavior also for the semi-implicit algorithm. This is demonstrated below by calculating the L_1 norm of the differences in the velocity components and pressure field from the analytical solution. The divergence in steady state velocity field is defined as the error in the continuity equation. Figure 6a plots these errors as a function of Δx on logarithmic scales for the three point distributions and a polynomial degree of 3. The best fit line for these 12 points is plotted. The slope of this line given by 3.47 signifies the order of convergence. Similarly, the orders of convergence are estimated for polynomial degrees of 4, 5 and 6 for the Courant number of 12 and presented in fig. 6. As expected, we observe that the slopes increase monotonically with the polynomial degree.



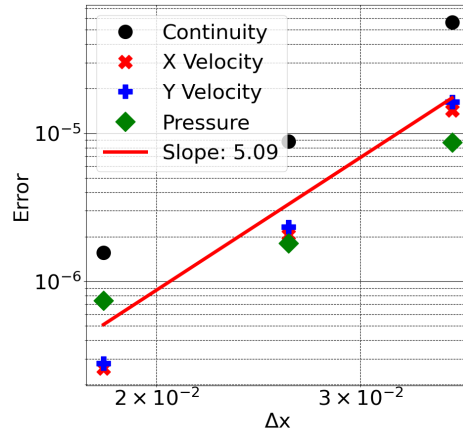
(a) Polynomial Degree 3



(b) Polynomial Degree 4



(c) Polynomial Degree 5



(d) Polynomial Degree 6

Figure 6: Errors for Semi-Implicit Algorithm: Courant No.: 12

For other Courant numbers, the slopes of the best fit lines are estimated similarly (not shown here). Figure 7 plots these orders of convergence for the fractional step method with Courant number of 0.8 and the semi-implicit method for the Courant numbers of 8 and 12. The expected orders of convergence for interpolation, gradient and Laplacian operators are $k + 1$, k and $k - 1$ respectively for a polynomial degree of k [45, 49]. It can be seen that

the order of convergence for the Navier-Stokes method, which has both gradient and Laplacian operators is between the three lines. As expected, the semi-implicit algorithm also has the same discretization error convergence properties of the fractional step method [45].

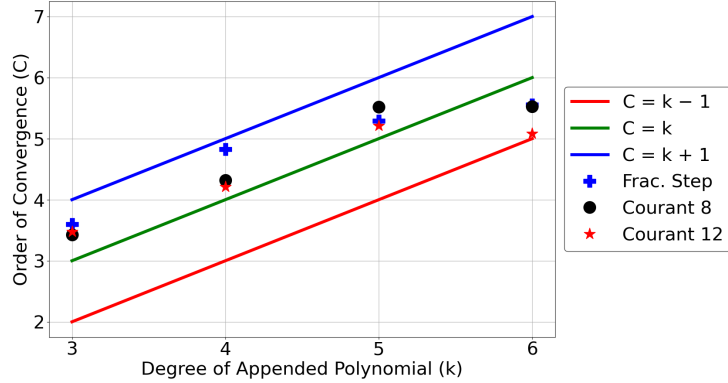


Figure 7: Order of Convergence with Polynomial Degree for Fractional Step [45] and Semi-Implicit Algorithms

4.2. Problem with a Temporal Decay of the Velocity Field

In this section, we analyze the discretization errors for a flow which decays with time to a null solution. The initial condition on a unit square domain is given by the following stream function [57]:

$$\Psi(x, y) = \frac{\sin^2(\pi x)\sin^2(\pi y)}{\pi} \quad (24)$$

The initial velocity field corresponding to this stream function is:

$$\begin{aligned} u(x, y) &= \frac{\partial \Psi}{\partial y} = \sin^2(\pi x)\sin(2\pi y) \\ v(x, y) &= -\frac{\partial \Psi}{\partial x} = -\sin(2\pi x)\sin^2(\pi y) \end{aligned} \quad (25)$$

The initial velocity field is divergence free. We set homogeneous Dirichlet boundary conditions on all four walls of the unit square. The Reynolds number is defined as $Re = \rho u_m L / \mu$ where, density ($\rho = 1$), maximum velocity ($u_m = 1$) and length of the square cavity ($L = 1$) are prescribed. Based on the prescribed Reynolds number of 100, the dynamic viscosity (μ) is computed. The initial velocity field is integrated in time till 0.5 seconds. Four different point distributions are used: [299, 673, 1503, 3404] points which correspond to an average Δx of [0.0614, 0.0409, 0.0274, 0.0183] respectively. Simulations with all these points distributions and polynomial degrees from 3 to 6 are performed with a fixed $\Delta t = 0.01$ seconds. After 0.5 seconds, the velocity components are interpolated to 100 uniform points along the horizontal and vertical center lines using the same PHS-RBF used for the solution. Let $[f^h, f^{2h}, f^{4h}]$ denote these interpolated velocities for three successive point distributions: [1503, 673, 299] and [3404, 1503, 673]. We assume that subtracting f^h from f^{2h} and f^{2h} from f^{4h} cancels the temporal error since a fixed Δt is used. Thus, using Richardson extrapolation, the spatial order of convergence is calculated as:

$$C = \log_2 \left(\frac{f^{4h} - f^{2h}}{f^{2h} - f^h} \right) \quad (26)$$

Equation (26) is applied to the L_1 norm of the differences between the interpolated velocities to estimate the order of convergence. These values are plotted in fig. 8 for both the triplets of point distributions. We again see that all the orders of convergence lie in the expected range of $C = k - 1$ to $C = k + 1$. As a structured Cartesian point layout is not used, the Δx is non-uniform. The slight deviations from the expected values may be attributed to the irregular point distributions. Moreover, the temporal errors may not

exactly cancel when the differences are computed as in eq. (26).

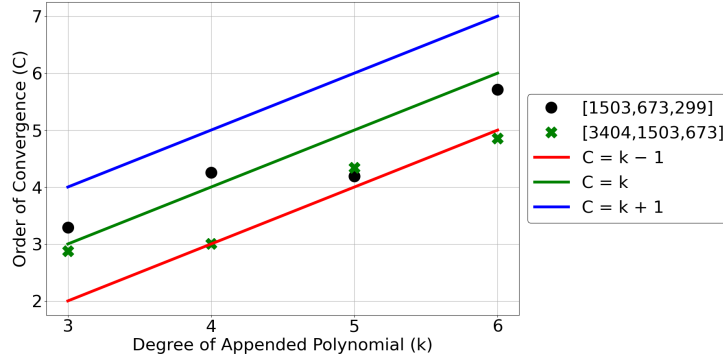


Figure 8: Order of Convergence with Polynomial Degree for Semi-Implicit Algorithm

5. Applications to Complex Flows

5.1. Wake of a Circular Cylinder in a Uniform Flow

Fluid flows over bluff bodies have been studied over several decades since they have many engineering applications. Here, we apply the semi-implicit algorithm to simulate flow over a circular cylinder. A schematic of the flow domain is shown in fig. 9. A uniform inlet flow of unit velocity is set at the left boundary. Homogeneous pressure boundary condition is applied on the right boundary with top and bottom boundaries set to symmetry conditions. No-penetration and no-slip boundary conditions are prescribed at the cylinder surface. Details of our implementation of these boundary conditions are described in section 3.1. The Reynolds number is defined as $Re = \rho U_i D / \mu$ where, density ρ , inlet velocity U_i and diameter D are all set to unity. The dynamic viscosity is estimated (μ) based on the prescribed value of the Reynolds number. The inlet is placed at an upstream distance of $20D$ from the cylinder center. The downstream distance is taken as $30D$.

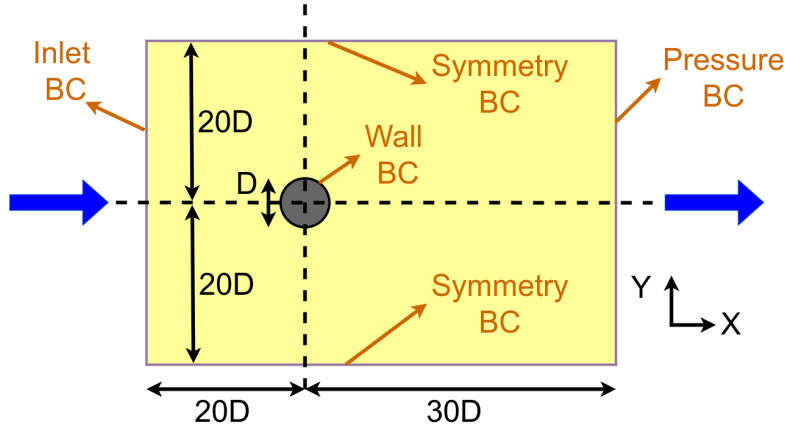


Figure 9: Domain with Diameter $D = 1$ (not to scale)

We first consider Reynolds numbers of 10, 20 and 30 which have a steady state solution [58–64]. Simulations are started with a uniform flow field in X direction. Time integration is performed using the BDF2 method as described in section 3 till the L_1 norm of the steady state error given by $\frac{\phi^{n+1}-\phi^n}{\Delta t}$ is less than $1E-6$. ϕ^{n+1} and ϕ^n denote the velocity fields at consecutive timesteps. Three different point distributions with [33704, 59573, 105534] points is considered which corresponds to average Δx of [0.24, 0.18, 0.13] respectively. Since the gradients are stronger near the cylinder, a non-uniform point distribution is generated using Gmsh [65] such that the points on and around the cylinder are 5 times more refined than those in the far upstream and downstream regions. This approach is computationally more efficient than a uniform point distribution. All the simulations are performed with polynomial degrees of 5 and 6 and a Courant number of 10. Figure 10 plots the variation of pressure over the cylindrical surface. It can be seen that grid independent solutions are obtained from the two finer point sets with Δx of 0.18 and 0.13. For the remaining steady state simulations, we

have used Δx of 0.13 and the polynomial degree of 6.

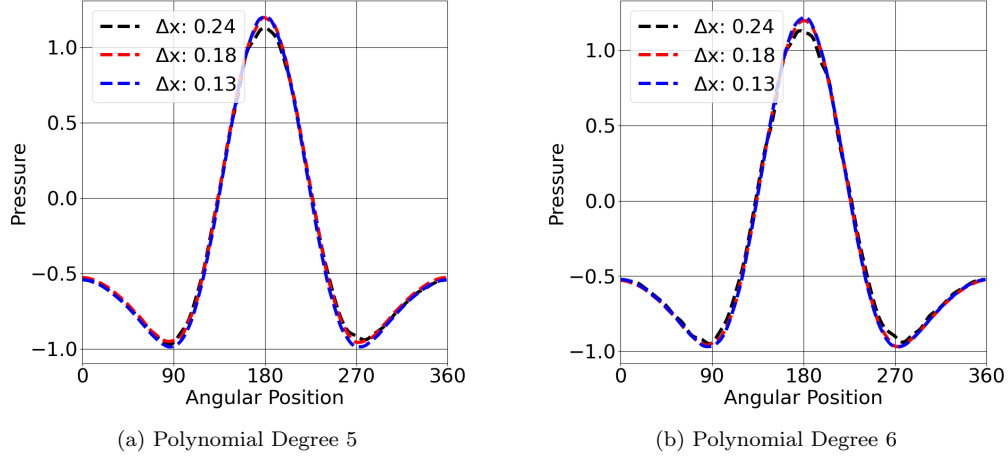


Figure 10: Grid Independence for $Re = 30$: Pressure Variation over Cylinder Surface

Total forces per unit length experienced by the cylinder in the X and Y directions are estimated by integrating the stress components over the surface:

$$\begin{aligned}
 F_x &= \frac{D}{2} \int_0^{2\pi} (\sigma_{xx} \cos \theta + \sigma_{yx} \sin \theta) d\theta \\
 F_y &= \frac{D}{2} \int_0^{2\pi} (\sigma_{yy} \sin \theta + \sigma_{xy} \cos \theta) d\theta
 \end{aligned} \tag{27}$$

where, components of the stress tensor ($\boldsymbol{\sigma}$) are given by:

$$\sigma_{xx} = -p + 2\mu \frac{\partial u}{\partial x} \quad \sigma_{yy} = -p + 2\mu \frac{\partial v}{\partial y} \quad \sigma_{xy} = \sigma_{yx} = \mu \left(\frac{\partial u}{\partial y} + \frac{\partial v}{\partial x} \right) \tag{28}$$

The pressure and strain rates are first interpolated to 360 uniform points along the cylindrical surface. Integrals in eq. (27) are estimated using the Simpson's rule [55] over these 360 points. The forces are non-dimensionalized

to compute the drag (C_D) and lift (C_L) coefficients:

$$C_D = \frac{F_x}{\rho U_i^2 D/2} \quad C_L = \frac{F_y}{\rho U_i^2 D/2} \quad (29)$$

Table 1 lists the drag coefficient and pressure values at the leading and lagging stagnation regions for three Reynolds numbers in the steady state regime. Comparison with seven previously published studies shows that the current estimates are within the expected ranges. It must be emphasized that despite extensive numerical simulations of the flow over a circular cylinder, there is no clear agreement among the various solutions, primarily because of the different computational domain sizes used, upstream distances and outflow boundary conditions. Our results are in close agreement with results of Dennis and Chang [64] for Re of 10 and 20, and with results of all three listed previous works for Re of 30.

Reynolds Number	Reference	Drag Coefficient	Pressure at theta=0	Pressure at theta=pi
10	Dennis and Chang [64]	2.846	-0.742	1.489
	Takami and Keller [58]	2.7541	-0.6702	1.4744
	Tuann and Olson [59]	3.177	-0.773	1.744
	Ding et al. [60]	3.07	-	-
	Present Work	2.877	-0.7121	1.516
20	Dennis and Chang [64]	2.045	-0.589	1.269
	Takami and Keller [58]	2.0027	-0.537	1.2612
	Tuann and Olson [59]	2.253	-0.614	1.457
	Fornberg [61]	2.0001	-0.57	1.28
	Ding et al. [60]	2.18	-	-
Present Work	2.072	-0.574	1.283	
30	Takami and Keller [58]	1.7167	-0.5304	1.1836
	Nieuwstadt and Keller [62]	1.7329	-0.5556	1.1765
	Gushchin and Shchennikov [63]	1.808	-	1.196
	Present Work	1.739	-0.5285	1.196

Table 1: Drag Coefficient and Stagnation Pressures for Steady State Flows

Next we present the results for Reynolds numbers of 100 and 200 for which there is temporal variation due to vortex shedding. For these cases, a point distribution with 163798 points corresponding to an average Δx of 0.10 with a polynomial degree of 6 is used. As described before, non-uniform points distribution is used for computational efficiency. Starting from a uniform velocity field, the equations are integrated in time till a stationary solution is obtained. Figure 11 plots the temporal variations of lift and drag coefficients for both the Reynolds numbers. Sinusoidal variations

are observed as expected [60]. The Strouhal number is computed from the frequency of the lift coefficient: $St = fD/U_i$. Table 2 documents the ranges of lift and drag coefficients together with the Strouhal numbers. As for the steady cases, present estimates fall within the documented ranges in the literature.

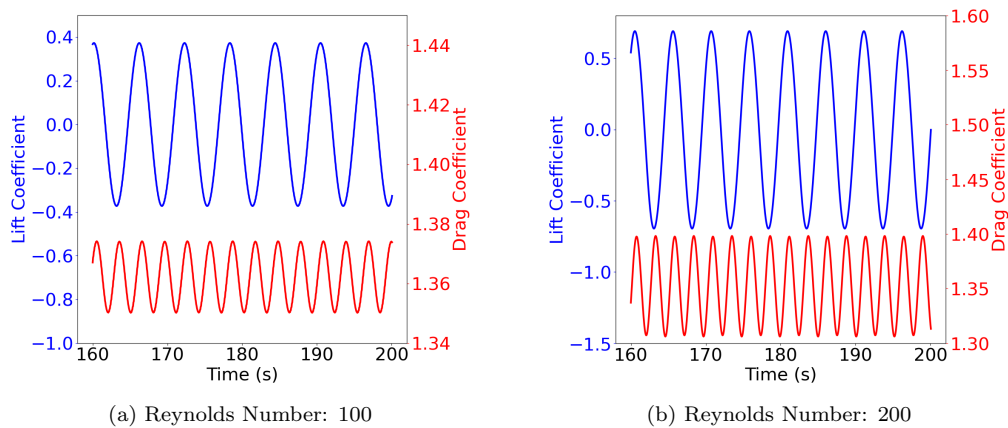


Figure 11: Lift and Drag Coefficients (163798 points, Average $\Delta x = 0.1105$, Degree of Appended Polynomial: 5)

Reynolds Number	Reference	Drag Coefficient	Lift Coefficient	Strouhal Number
100	Braza et al. [66]	1.364 ± 0.015	± 0.25	0.16
	Liu et al. [67]	1.35 ± 0.012	± 0.339	0.165
	Ding et al. [60]	1.325 ± 0.008	± 0.28	0.164
	Present Work	1.362 ± 0.0118	± 0.3331	0.1649
200	Belov et al. [68]	1.19 ± 0.042	± 0.64	
	Braza et al. [66]	1.4 ± 0.05	± 0.75	0.193
	Liu et al. [67]	1.31 ± 0.049	± 0.69	0.192
	Ding et al. [60]	1.327 ± 0.045	± 0.60	0.196
	Present Work	1.353 ± 0.0448	± 0.6931	0.1963

Table 2: Strouhal Number, Drag and Lift Coefficients for Unsteady Flows

5.2. Couette Flow in an Ellipse with Two Rotating Inner Cylinders

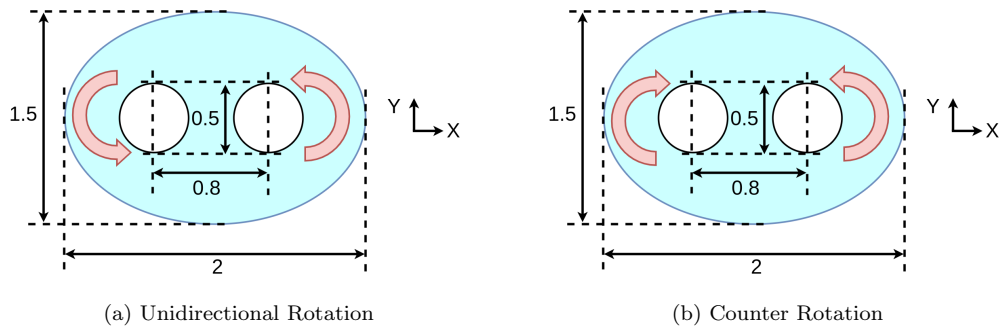


Figure 12: Geometry

We next present results of a Couette flow generated by two rotating circular cylinders inside a stationary elliptical enclosure. The fluid is initially at rest in the annular region between the cylinders. Figure 12a shows the

domain with dimensions in which both the cylinders rotate in the counter-clockwise direction and fig. 12b shows the case with cylinders rotating in opposite directions. A rotational velocity (ω) of 1 radians per second is set at both the inner cylinders. The Reynolds number is defined with respect to the radius of the inner cylinder and its velocity: $Re = \rho\omega r_i^2/\mu$ where, $\omega = 1$, $\rho = 1$, $r_i = 0.25$ and μ is computed based on the Reynolds number. We have prescribed a Reynolds number of 40 for which we see a steady two dimensional flow.

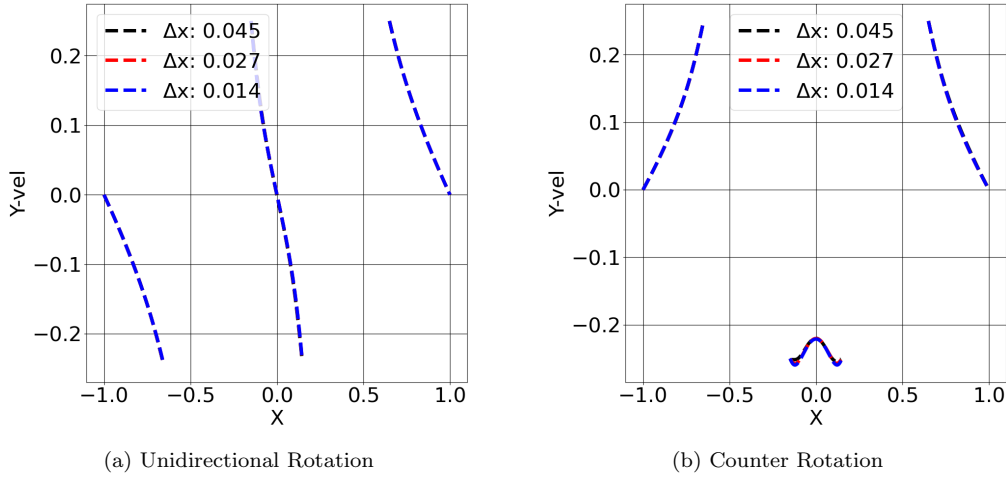


Figure 13: Grid Independence for Polynomial Degree 5: Y-Vel along Horizontal Center Line

We have simulated the flows using three point distributions with 1021, 2748 and 10843 points which correspond to average Δx values of 0.045, 0.027 and 0.014. We have used a polynomial degree of 5 for all the simulations. Figure 13 shows that the Y component of the velocity along the horizontal center lines overlap. The finest point set is used for all the subsequent simulations. Figure 14 plots convergence of the steady state error with timestep

for the polynomial degree of 5. Similar to the plots shown in section 4.1, the case with higher Δx converges to steady state in less number of timesteps for the same Courant number.

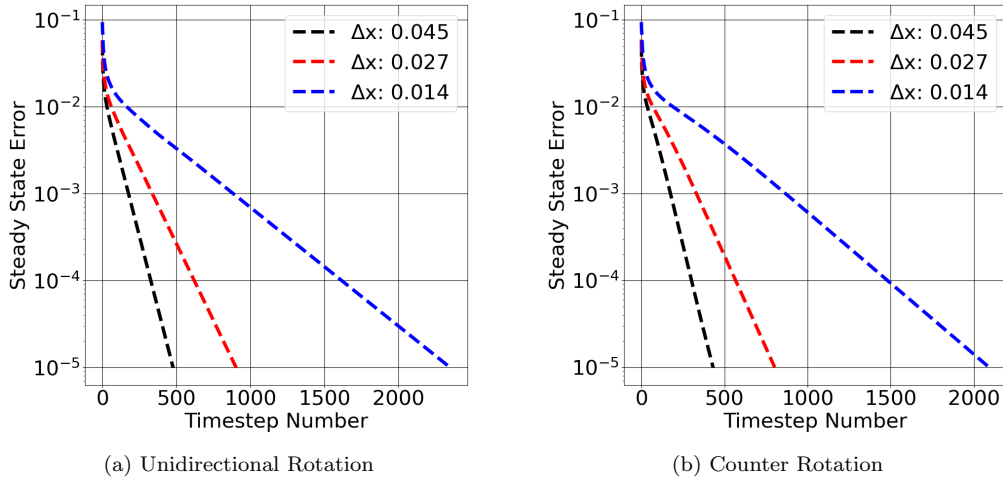


Figure 14: Convergence of the Semi-Implicit Algorithm with Polynomial Degree 5 and Courant No. 10

Figure 15 plots the contours of pressure superposed with streamlines. For the case of unidirectional rotation, a stagnation point is formed between the cylinders as the velocities are in opposite directions in that region. On the other hand, in the case of counter rotation, the velocities add in the region between the two cylinders. Thus, we see a region of low pressure between the the cylinders and a stagnation high pressure region on the bottom wall.

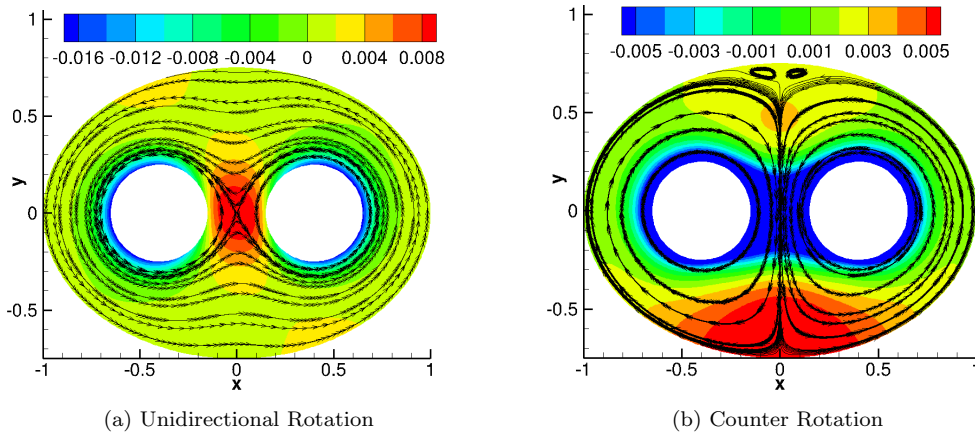


Figure 15: Contours of Pressure with Streamlines

5.3. Flow in a Periodic Bellowed Channel

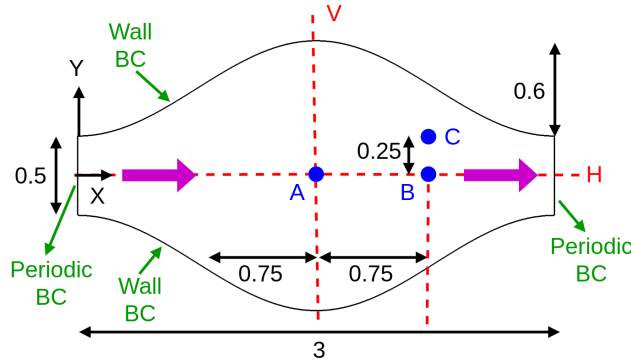


Figure 16: Geometry of the Bellowed Channel

Figure 16 shows the dimensions of a sinusoidal bellow with fluid flowing from left to right [69, 70]. The top and bottom boundaries are walls with no-slip and no-penetration conditions. Periodicity is prescribed on the left and right boundaries as described in section 3.1. Velocity fields are interpolated on uniform points along a horizontal and vertical center lines for analysis. Similarly, temporal variations of the fields at three reference points A, B

and C are also plotted. The minimum width of the channel used as the characteristic length (L) is set to 0.5 and density (ρ) is set to unity. The periodic flow is driven with a mean pressure gradient in the X direction:

$$\frac{\partial \bar{p}}{\partial x} = \frac{12\mu}{L^2} \quad (30)$$

Velocity in the X direction averaged over the minimum width at the left boundary is used to calculate the flow Reynolds number: $Re = \frac{\rho \bar{u} L}{\mu}$. Simulations are performed for two different viscosity values: 0.01 and 0.002 which correspond to Reynolds numbers of 55.6 and 172.9 respectively. We find that 55.6 gives a steady state flow whereas, 172.9 generates an unsteady flow. Both the simulations are started with a zero initial condition and integrated in time till stationary fields are obtained.

Three different point distributions with 3626, 6367 and 9778 points which correspond to average Δx of 0.032, 0.024 and 0.019 respectively are used with a polynomial degree of 5. The X component of velocity and vorticity are plotted along the horizontal and vertical center lines in fig. 17. It can be seen that the line plots for all the point distributions overlap. For all the simulations in this section, we use the finest distribution with 9778 points and average $\Delta x = 0.019$.

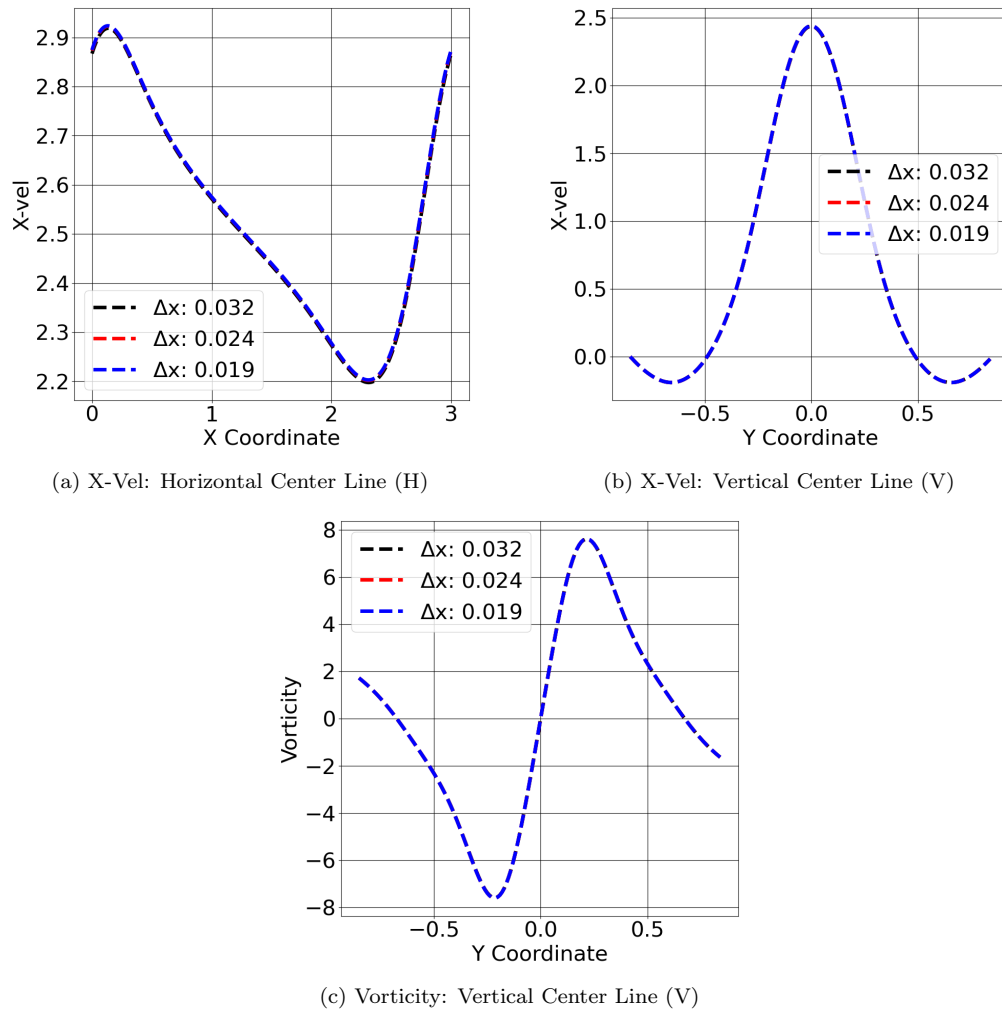


Figure 17: Grid Independence for $Re = 55.6$ with Polynomial Degree 5

Figure 18 plots the contours for the Reynolds number of 55.6. A steady state solution is obtained for this case. Note that since a mean pressure gradient (eq. (30)) is applied as a force in the X-momentum equation, pressure perturbations on top of the mean pressure are plotted in fig. 18c together with streamlines. As expected, the steady flow is symmetric with respect to the horizontal center line.

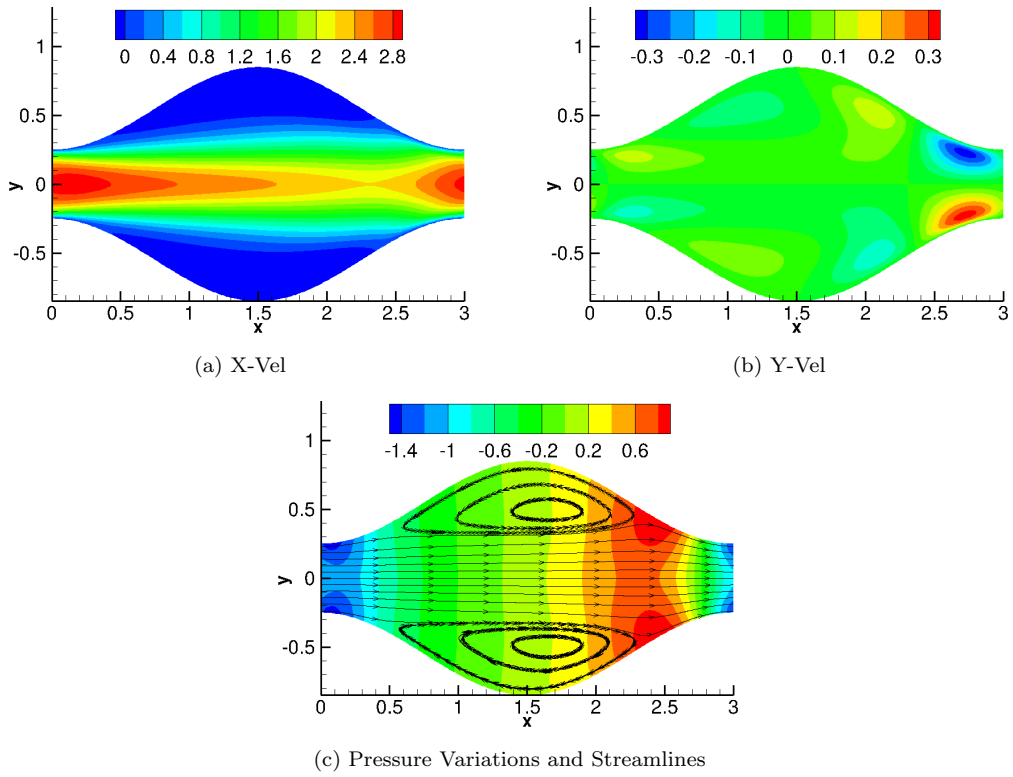


Figure 18: Contour Plots for $Re = 55.6$ ($\Delta x = 0.019$ with Polynomial Degree 5)

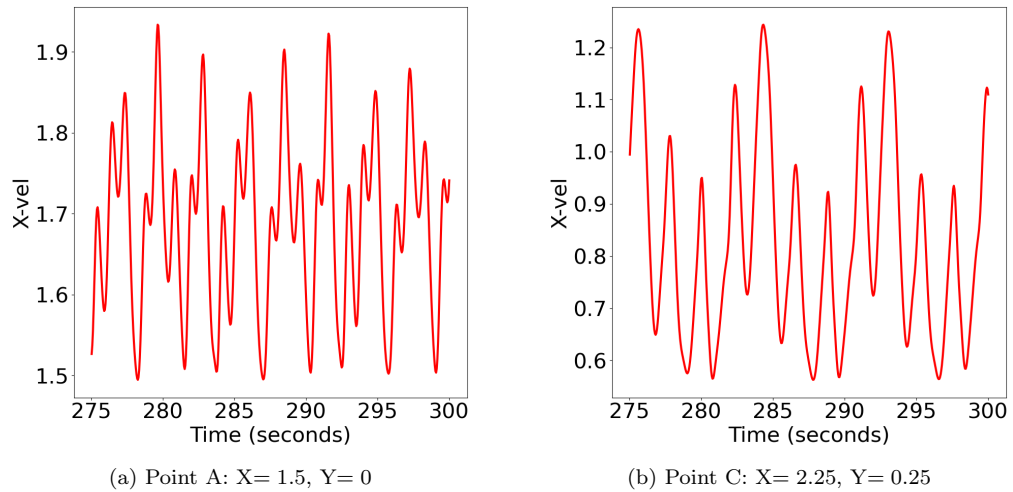


Figure 19: Temporal Variation of X-Vel for $Re = 172.9$

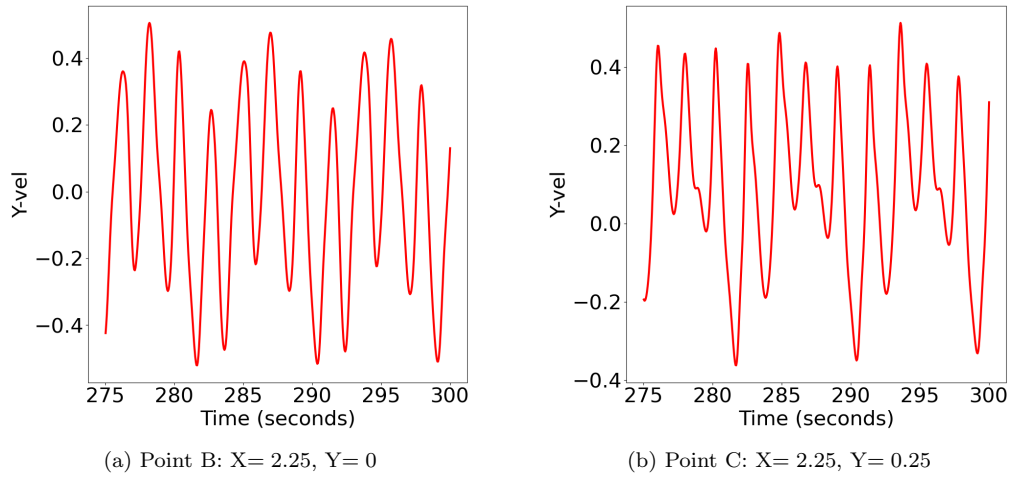


Figure 20: Temporal Variation of Y-Vel for $Re = 172.9$

Figures 19 and 20 plot the temporal variation of the velocity components at the three points A, B and C marked in fig. 16 for the Reynolds number of 172.9. We observe that the X-velocity oscillates around a mean positive value since the flow direction is from left to right. The mean value at point C is lower than the point A which is along the horizontal center line. The Y-velocity on the other hand oscillates around a mean of zero at both points B and C. Multiple frequencies are observed in the velocity signals at the points A, B and C. Figure 21 plots the contours of the excess pressure over the mean gradient superposed with streamlines at various time instants after a stationary solution is obtained. We see multiple vortices oscillating with time.

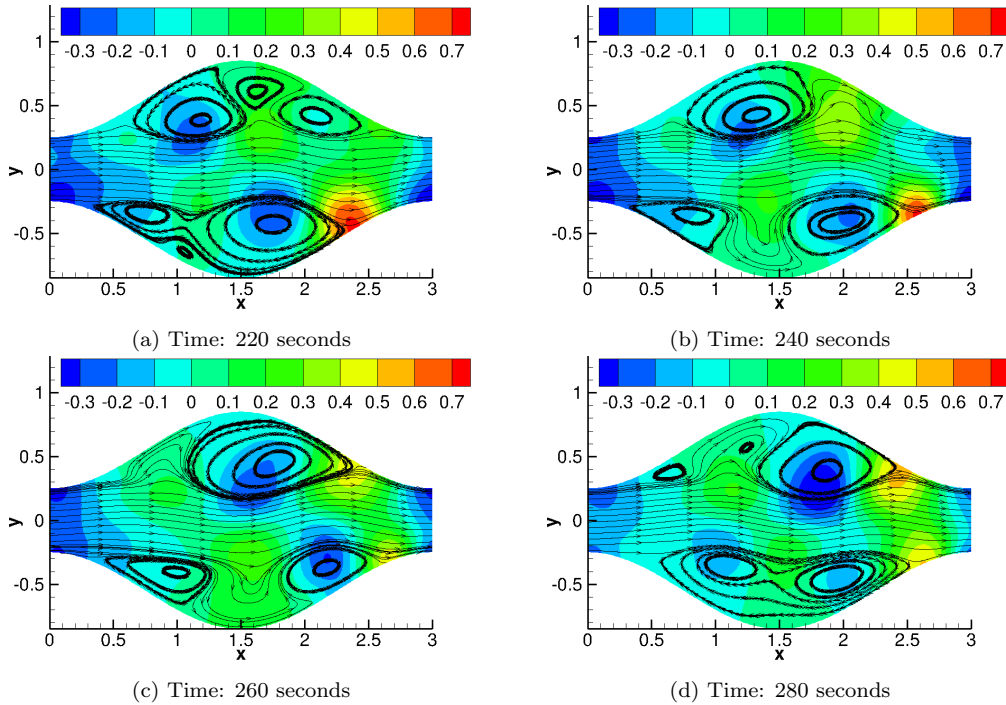


Figure 21: Contours of Excess Pressure over Mean Gradient with Streamlines for $Re=172.9$ at Various Time Instants

6. Summary

A meshless semi-implicit iterative algorithm for the solution of incompressible Navier-Stokes equations is presented. The PHS-RBFs with appended polynomials give exponential order of convergence for the degree of the appended polynomial. The BDF2 scheme is used for temporal integration of the momentum equations. A Poisson equation for pressure corrections is formulated by imposing divergence free condition on the iterated velocity field. At each time step, the momentum and pressure correction equations are repeatedly solved until the velocities and pressure converge to a pre-specified tolerance. We demonstrate that this semi-implicit procedure is stable and

convergent for high Courant numbers.

In this paper, we have demonstrated the convergence and discretization accuracy of the algorithm for two model problems and simulated three other complex problems. In all cases, the algorithm is stable for Courant numbers in excess of ten. No additional under-relaxation is needed to converge the nonlinearities and coupling between the equations. The model problems include a circular Couette flow with exact analytical solution, and the decay of an initial flow field to a null solution. In both cases, we demonstrate the exponential convergence of the discretization error per the degree of the appended polynomial. Comparison of the CPU runtimes with the previously published fractional step method [45] shows that this algorithm is around 5 to 6 times faster for the Courant number of 12. Subsequently, both steady and unsteady flows over a circular cylinder are simulated and the lift and drag coefficients are compared with values in the literature. The method is also applied to simulate two practical problems. The first problem deals with flow in the gap formed between two rotating circular cylinders and a stationary outer ellipse. Results are presented for the cases of unidirectional and counter rotations. Next we have simulated flow inside a sinusoidal bellow with periodic boundary conditions. Two Reynolds numbers are considered showing steady and unsteady flows. The unsteady case shows complex flow patterns with multiple oscillating vortices. For all these problems, a systematic grid independence study followed by line and contour plots are presented. These are in qualitative agreement with published results in literature.

The algorithm has a potential to accurately and efficiently solve many fluid flow and heat transfer problems in complex domains. An open source

code Meshless Multi-Physics Software (MeMPhyS) [1] is available for interested users of the algorithm. Future extensions will include a parallel implementation of the software on high-performance CPUs and GPUs and implementation of different physical models for turbulence and multiple phases.

References

- [1] S. Shahane, S. P. Vanka, MeMPhyS: Meshless Multi-Physics Software, 2021. URL: <https://github.com/shahaneshantanu/memphys>.
- [2] F. Harlow, J. Welch, Numerical calculation of time-dependent viscous incompressible flow of fluid with free surface, *The Physics of Fluids* 8 (1965) 2182–2189.
- [3] A. J. Chorin, Numerical solution of the navier-stokes equations, *Mathematics of computation* 22 (1968) 745–762.
- [4] R. Temam, Approximation of the solution of the navier- stokes equations by the fractional step method(approximate solution method for navier-stokes equations for incompressible viscous fluids), *Archive for Rational Mechanics and Analysis* 32 (1969) 135–153.
- [5] J. Kim, P. Moin, Application of a fractional-step method to incompressible navier-stokes equations, *Journal of computational physics* 59 (1985) 308–323.
- [6] M. Rosenfeld, D. Kwak, M. Vinokur, A fractional step solution method for the unsteady incompressible navier-stokes equations in generalized

- coordinate systems, *Journal of Computational Physics* 94 (1991) 102–137.
- [7] S. Shahane, N. Aluru, P. Ferreira, S. G. Kapoor, S. P. Vanka, Finite volume simulation framework for die casting with uncertainty quantification, *Applied Mathematical Modelling* 74 (2019) 132–150.
- [8] R. I. Issa, Solution of the implicitly discretised fluid flow equations by operator-splitting, *Journal of computational physics* 62 (1986) 40–65.
- [9] J. P. Van Doormaal, G. D. Raithby, Enhancements of the simple method for predicting incompressible fluid flows, *Numerical heat transfer* 7 (1984) 147–163.
- [10] S. V. Patankar, D. B. Spalding, A calculation procedure for heat, mass and momentum transfer in three-dimensional parabolic flows, in: *Numerical prediction of flow, heat transfer, turbulence and combustion*, Elsevier, 1983, pp. 54–73.
- [11] S. V. Patankar, V. S. Prataap, D. B. Spalding, Prediction of laminar flow and heat transfer in helically coiled pipes, in: *Numerical Prediction of Flow, Heat Transfer, Turbulence and Combustion*, Elsevier, 1983, pp. 117–129.
- [12] S. V. Patankar, *Numerical heat transfer and fluid flow*, Taylor & Francis, 2018.
- [13] S. P. Vanka, Block-implicit calculation of steady turbulent recirculating flows, *International journal of heat and mass transfer* 28 (1985) 2093–2103.

- [14] M. Braaten, S. V. Patankar, Fully coupled solution of the equations for incompressible recirculating flows using a penalty-function finite-difference formulation, *Computational mechanics* 6 (1990) 143–155.
- [15] M. Darwish, I. Sraj, F. Moukalled, A coupled finite volume solver for the solution of incompressible flows on unstructured grids, *Journal of Computational Physics* 228 (2009) 180–201.
- [16] S. P. Vanka, G. Leaf, Fully-coupled solution of pressure-linked fluid flow equations, Technical Report, Argonne National Lab., IL (USA), 1983.
- [17] Z. Chen, A. Przekwas, A coupled pressure-based computational method for incompressible/compressible flows, *Journal of Computational Physics* 229 (2010) 9150–9165.
- [18] A. Sohankar, The les and dns simulations of heat transfer and fluid flow in a plate-fin heat exchanger with vortex generators (2004).
- [19] M. Manhart, A zonal grid algorithm for dns of turbulent boundary layers, *Computers & Fluids* 33 (2004) 435–461.
- [20] S. Ha, J. Park, D. You, A gpu-accelerated semi-implicit fractional-step method for numerical solutions of incompressible navier–stokes equations, *Journal of Computational Physics* 352 (2018) 246–264.
- [21] G. Kalitzin, X. Wu, P. A. Durbin, Dns of fully turbulent flow in a lpt passage, *International Journal of Heat and Fluid Flow* 24 (2003) 636–644.

- [22] J. You, H. Choi, J. Y. Yoo, A modified fractional step method of keeping a constant mass flow rate in fully developed channel and pipe flows, *KSME international journal* 14 (2000) 547–552.
- [23] J. Robichaux, S. Balachandar, S. P. Vanka, Three-dimensional floquet instability of the wake of square cylinder, *Physics of Fluids* 11 (1999) 560–578.
- [24] NEK: a fast and scalable high-order solver for computational fluid dynamics, 2021. URL: <https://github.com/Nek5000>.
- [25] P. R. Spalart, R. D. Moser, M. M. Rogers, Spectral methods for the navier-stokes equations with one infinite and two periodic directions, *Journal of Computational Physics* 96 (1991) 297–324.
- [26] D. Tafti, S. P. Vanka, A numerical study of the effects of spanwise rotation on turbulent channel flow, *Physics of Fluids A: Fluid Dynamics* 3 (1991) 642–656.
- [27] D. Tafti, S. P. Vanka, A three-dimensional numerical study of flow separation and reattachment on a blunt plate, *Physics of Fluids A: Fluid Dynamics* 3 (1991) 2887–2909.
- [28] R. P. Pawlowski, J. N. Shadid, J. P. Simonis, H. F. Walker, Globalization techniques for newton–krylov methods and applications to the fully coupled solution of the navier–stokes equations, *SIAM review* 48 (2006) 700–721.

- [29] D. A. Knoll, D. E. Keyes, Jacobian-free newton–krylov methods: a survey of approaches and applications, *Journal of Computational Physics* 193 (2004) 357–397.
- [30] S. P. Vanka, Block-implicit multigrid calculation of two-dimensional recirculating flows, *Computer Methods in Applied Mechanics and Engineering* 59 (1986) 29–48.
- [31] S. P. Vanka, Block-implicit multigrid solution of navier-stokes equations in primitive variables, *Journal of Computational Physics* 65 (1986) 138–158.
- [32] V. John, L. Tobiska, Numerical performance of smoothers in coupled multigrid methods for the parallel solution of the incompressible navier–stokes equations, *International Journal for Numerical Methods in Fluids* 33 (2000) 453–473.
- [33] J. Monaghan, Smoothed particle hydrodynamics and its diverse applications, *Annual Review of Fluid Mechanics* 44 (2012) 323–346.
- [34] N. Perrone, R. Kao, A general finite difference method for arbitrary meshes, *Computers & Structures* 5 (1975) 45–57.
- [35] W. Liu, S. Jun, Y. Zhang, Reproducing kernel particle methods, *International journal for numerical methods in fluids* 20 (1995) 1081–1106.
- [36] T. Belytschko, Y. Lu, L. Gu, Element-free galerkin methods, *International journal for numerical methods in engineering* 37 (1994) 229–256.

- [37] T. Liszka, C. Duarte, W. Tworzydło, hp-meshless cloud method, *Computer Methods in Applied Mechanics and Engineering* 139 (1996) 263–288.
- [38] I. Babuška, J. Melenk, The partition of unity method, *International journal for numerical methods in engineering* 40 (1997) 727–758.
- [39] E. Oñate, S. Idelsohn, O. Zienkiewicz, R. Taylor, A finite point method in computational mechanics. applications to convective transport and fluid flow, *International journal for numerical methods in engineering* 39 (1996) 3839–3866.
- [40] C. Shu, H. Ding, K. Yeo, Local radial basis function–based differential quadrature method and its application to solve two–dimensional incompressible navier–stokes equations, *Computer methods in applied mechanics and engineering* 192 (2003) 941–954.
- [41] H. Ding, C. Shu, K. Yeo, D. Xu, Numerical computation of three–dimensional incompressible viscous flows in the primitive variable form by local multiquadric differential quadrature method, *Computer Methods in Applied Mechanics and Engineering* 195 (2006) 516–533.
- [42] Y. Sanyasiraju, G. Chandhini, Local radial basis function based gridfree scheme for unsteady incompressible viscous flows, *Journal of Computational Physics* 227 (2008) 8922–8948.
- [43] A. Vidal, A. Kassab, E. Divo, A direct velocity–pressure coupling Meshless algorithm for incompressible fluid flow simulations, *Engineering Analysis with Boundary Elements* 72 (2016) 1–10.

- [44] R. Zamolo, E. Nobile, Solution of incompressible fluid flow problems with heat transfer by means of an efficient RBF–FD meshless approach, *Numerical Heat Transfer, Part B: Fundamentals* (2019) 1–24.
- [45] S. Shahane, A. Radhakrishnan, S. P. Vanka, A high-order accurate meshless method for solution of incompressible fluid flow problems, *arXiv preprint arXiv:2010.01702* (2020).
- [46] V. Bayona, N. Flyer, B. Fornberg, G. A. Barnett, On the role of polynomials in rbf-fd approximations: Ii. numerical solution of elliptic pdes, *Journal of Computational Physics* 332 (2017) 257–273.
- [47] G. Kosec, B. Šarler, Solution of thermo-fluid problems by collocation with local pressure correction, *International Journal of Numerical Methods for Heat & Fluid Flow* (2008).
- [48] G. Kosec, J. Slak, Radial basis function-generated finite differences solution of natural convection problem in 3d, in: *AIP Conference Proceedings*, volume 2293, AIP Publishing LLC, 2020, p. 420094.
- [49] N. Flyer, B. Fornberg, V. Bayona, G. Barnett, On the role of polynomials in RBF–FD approximations: I. Interpolation and accuracy, *Journal of Computational Physics* 321 (2016) 21–38.
- [50] A. Radhakrishnan, M. Xu, S. Shahane, S. P. Vanka, A non-nested multilevel method for meshless solution of the poisson equation in heat transfer and fluid flow, *arXiv preprint arXiv:2104.13758* (2021).
- [51] R. Hardy, Multiquadric equations of topography and other irregular surfaces, *Journal of geophysical research* 76 (1971) 1905–1915.

- [52] E. Kansa, Multiquadrics—A scattered data approximation scheme with applications to computational fluid-dynamics—I surface approximations and partial derivative estimates, *Computers & Mathematics with applications* 19 (1990) 127–145.
- [53] E. Kansa, Multiquadrics—A scattered data approximation scheme with applications to computational fluid-dynamics—II solutions to parabolic, hyperbolic and elliptic partial differential equations, *Computers & mathematics with applications* 19 (1990) 147–161.
- [54] E. Kansa, Y. Hon, Circumventing the ill-conditioning problem with multiquadric radial basis functions: applications to elliptic partial differential equations, *Computers & Mathematics with applications* 39 (2000) 123–137.
- [55] E. Süli, D. F. Mayers, *An introduction to numerical analysis*, Cambridge university press, 2003.
- [56] R. J. LeVeque, *Finite difference methods for ordinary and partial differential equations: steady-state and time-dependent problems*, SIAM, 2007.
- [57] J. B. Bell, P. Colella, H. M. Glaz, A second-order projection method for the incompressible navier-stokes equations, *Journal of Computational Physics* 85 (1989) 257–283.
- [58] H. Takami, H. B. Keller, Steady two-dimensional viscous flow of an incompressible fluid past a circular cylinder, *The Physics of Fluids* 12 (1969) II–51.

- [59] S.-Y. Tuann, M. D. Olson, Numerical studies of the flow around a circular cylinder by a finite element method, *Computers & Fluids* 6 (1978) 219–240.
- [60] H. Ding, C. Shu, K. Yeo, D. Xu, Simulation of incompressible viscous flows past a circular cylinder by hybrid fd scheme and meshless least square-based finite difference method, *Computer Methods in Applied Mechanics and Engineering* 193 (2004) 727–744.
- [61] B. Fornberg, A numerical study of steady viscous flow past a circular cylinder, *Journal of Fluid Mechanics* 98 (1980) 819–855.
- [62] F. Nieuwstadt, H. Keller, Viscous flow past circular cylinders, *Computers & Fluids* 1 (1973) 59–71.
- [63] V. A. Gushchin, V. Shchennikov, A numerical method of solving the navier-stokes equations, *USSR Computational Mathematics and Mathematical Physics* 14 (1974) 242–250.
- [64] S. Dennis, G.-Z. Chang, Numerical solutions for steady flow past a circular cylinder at reynolds numbers up to 100, *Journal of Fluid Mechanics* 42 (1970) 471–489.
- [65] C. Geuzaine, J. Remacle, Gmsh: A 3-d finite element mesh generator with built-in pre-and post-processing facilities, *International Journal for Numerical Methods in Engineering* 79 (2009) 1309–1331.
- [66] M. Braza, P. Chassaing, H. H. Minh, Numerical study and physical analysis of the pressure and velocity fields in the near wake of a circular cylinder, *Journal of fluid mechanics* 165 (1986) 79–130.

- [67] C. Liu, X. Zheng, C. Sung, Preconditioned multigrid methods for unsteady incompressible flows, *Journal of Computational physics* 139 (1998) 35–57.
- [68] A. Belov, L. Martinelli, A. Jameson, A new implicit algorithm with multigrid for unsteady incompressible flow calculations, in: *33rd Aerospace sciences meeting and exhibit*, 1995, p. 49.
- [69] G. Wang, S. P. Vanka, Convective heat transfer in periodic wavy passages, *International Journal of Heat and Mass Transfer* 38 (1995) 3219–3230.
- [70] K. Stephanoff, I. J. Sobey, B. Bellhouse, On flow through furrowed channels. part 2. observed flow patterns, *Journal of Fluid Mechanics* 96 (1980) 27–32.